

## Flash ionization signatures in the type Ibn supernova SN 2019uo

ANJASHA GANGOPADHYAY,<sup>1,2</sup> KUNTAL MISRA,<sup>1,3</sup> DAICHI HIRAMATSU,<sup>4,5</sup> SHAN-QIN WANG,<sup>6</sup> GRIFFIN HOSSEINZADEH,<sup>7</sup> XIAOFENG WANG,<sup>8</sup> STEFANO VALENTI,<sup>3</sup> JUIA ZHANG,<sup>9</sup> D. ANDREW HOWELL,<sup>4,5</sup> LAIR ARCAVI,<sup>10,11</sup> G.C. ANUPAMA,<sup>12</sup> JAMISON BURKE,<sup>4,5</sup> RAYA DASTIDAR,<sup>1,13</sup> KOICHI ITAGAKI,<sup>14</sup> BRAJESH KUMAR,<sup>12</sup> BRIJESH KUMAR,<sup>1</sup> LONG LI,<sup>6</sup> CURTIS MCCULLY,<sup>4,5</sup> JUN MO,<sup>8</sup> SHASHI BHUSHAN PANDEY,<sup>1</sup> CRAIG PELLEGRINO,<sup>4,5</sup> HANNA SAI,<sup>8</sup> D.K. SAHU,<sup>12</sup> PANKAJ SANWAL,<sup>1,2</sup> AVINASH SINGH,<sup>12,15</sup> MRIDWEEKA SINGH,<sup>16,1</sup> JICHENG ZHANG,<sup>8</sup> TIANMENG ZHANG,<sup>17</sup> AND XINHAN ZHANG<sup>8</sup>

<sup>1</sup>Aryabhatta Research Institute of observational sciencES, Manora Peak, Nainital 263 002 India

<sup>2</sup>School of Studies in Physics and Astrophysics, Pandit Ravishankar Shukla University, Chattisgarh 492 010, India

<sup>3</sup>Department of Physics, University of California, 1 Shields Ave, Davis, CA 95616-5270, USA

<sup>4</sup>Las Cumbres Observatory, 6740 Cortona Drive Suite 102, Goleta, CA, 93117-5575 USA

<sup>5</sup>Department of Physics, University of California, Santa Barbara, CA 93106-9530, USA

<sup>6</sup>Guangxi Key Laboratory for Relativistic Astrophysics, School of Physical Science and Technology, Guangxi University, Nanning 530004, People's Republic of China

<sup>7</sup>Center for Astrophysics | Harvard & Smithsonian, 60 Garden Street, Cambridge, MA 02138-1516, USA

<sup>8</sup>Physics Department and Tsinghua Center for Astrophysics, Tsinghua University, China

<sup>9</sup>Yunnan Astronomical Observatory of China, Chinese Academy of Sciences, Kunming, 650011, China

<sup>10</sup>The School of Physics and Astronomy, Tel Aviv University, Tel Aviv 69978, Israel

<sup>11</sup>CIFAR Azrieli Global Scholars program, CIFAR, Toronto, Canada

<sup>12</sup>Indian Institute of Astrophysics, Koramangala 2nd Block, Bangalore 560034, India

<sup>13</sup>Department of Physics & Astrophysics, University of Delhi, Delhi-110 007

<sup>14</sup>Itagaki Astronomical Observatory, Japan

<sup>15</sup>Joint Astronomy Programme, Department of Physics, Indian Institute of Science, Bengaluru 560012, India

<sup>16</sup>Korea Astronomy and Space Science Institute, 776 Daedeokdae-ro, Yuseong-gu, Daejeon 34055, Republic of Korea

<sup>17</sup>National Astronomical Observatory of China, Chinese Academy of Sciences, Beijing, 100012, China

### ABSTRACT

We present photometric and spectroscopic observations of the type Ibn supernova (SN) 2019uo, the second ever SN Ibn with flash ionization (He II, C III, N III) features in its early spectra. SN 2019uo displays a rapid post-peak luminosity decline of 0.1 mag d<sup>-1</sup> similar to most of the SNe Ibn, but is fainter ( $M_{max}^V = -18.30 \pm 0.24$  mag) than a typical SN Ibn and shows a color evolution that places it between SNe Ib and the most extreme SNe Ibn. SN 2019uo shows P-cygni He I features in the early spectra which gradually evolves and becomes emission dominated post peak. It also shows faster evolution in line velocities as compared to most other members of the type Ibn subclass. The bolometric light curve is fairly described by a <sup>56</sup>Ni + circumstellar interaction model.

**Keywords:** supernovae: general – supernovae: individual: SN 2019uo – galaxies: individual: – techniques: photometric – techniques: spectroscopic

### 1. INTRODUCTION

Supernovae (SNe) undergoing interaction with a circumstellar medium (CSM) provide a unique window in the evolutionary phases of stars. Interaction, in general, produces narrow emission lines — broader than H II

regions but narrower than lines arising from the outer ejecta of the supernova (Hosseinzadeh et al. 2017). However, in some cases interaction happens below the photosphere without any observable narrow emission lines (e.g. Morozova et al. 2017; Andrews & Smith 2018). SNe IIn (Schlegel 1990) and SNe Ia-CSM display narrow H lines indicative of interaction with a H-rich CSM. Approximately 1% of core-collapse SNe (CCSNe) show little H and narrow He features ( $\sim 2000$  km s<sup>-1</sup>). With the discovery of SN 2006jc, Pastorello et al. (2007) in-

roduced this class as SNe Ibn, whose spectral features show interaction signatures between SN ejecta and a He-rich CSM. This is defined in analogy with SNe IIn, which show narrow H features (Schlegel 1990). SNe that are embedded in dense CSM may also show short-lived narrow high ionization emission lines ( $\leq 10$  days) owing to the recombination of the CSM following the shock breakout flash. These features are known as “flash features” (e.g. Gal-Yam et al. 2014). Hosseinzadeh et al. (2017) analysed a sample of SN Ibn light curves and showed that unlike SNe IIn, SNe Ibn are rather uniform in their light curve shape with rapid decay rates of  $0.05\text{--}0.15\text{ mag d}^{-1}$ . SNe Ibn may have double-peaked light curves like SNe IIn, but they show a faster rise than SNe IIn (Hosseinzadeh et al. 2017). On the other hand, Pastorello et al. (2016) showed that the class is heterogeneous with many outliers: OGLE-2012-SN-006 (Pastorello et al. 2015a) has a very slow decline; LSQ13ccw (Pastorello et al. 2015b) is faint and fast-declining; SNe 2005la and 2011hw (Pastorello et al. 2015c) are transitional type IIn/Ibn events; SN 2010al (Pastorello et al. 2015c) is the earliest detected SN Ibn with a slow rise and decline. Karamahmetoglu et al. (2019) recently identified a rapid evolving SN 2018bcc. SNe Ibn have bluer continuum than other CCSNe. Some SNe Ibn show P Cygni He I emission, while others transition from narrow to intermediate-width He I emissions (Hosseinzadeh et al. 2017).

So far, only indirect progenitor constraints for SNe Ibn are available. Pastorello et al. (2007) suggest Wolf-Rayet (WR) H-free atmospheres generate the He-rich CSM. The best studied case for unstable mass loss from a WR progenitor is SN 2006jc, for which an optical transient was detected at the SN location two years prior to explosion (Foley et al. 2007; Pastorello et al. 2007; Smith et al. 2008). Alternatively, CSM can be produced by stripping material from envelopes of massive binaries (Foley et al. 2007). However, a low-mass progenitor has been suggested for PS1-12sk, which occurred in a non-star-forming host (Sanders et al. 2013; Hosseinzadeh et al. 2019) — unlikely for a CCSN ( $\leq 0.2\%$ ; Hakobyan et al. 2012). A very recent study by Sun et al. (2019) for SNe 2006jc and 2015G implies an interacting binary progenitor scenario, based on late time UV/optical *HST* images.

In this paper we study the evolution of one such type Ibn SN 2019uo which was discovered on 2019 January 17.8 UT (JD 2458501.3) by Koichi Itagaki at R.A. =  $12^{\text{h}}02^{\text{m}}36.5^{\text{s}}$ , Decl. =  $+41^{\circ}03'42''$  (J2000.0). The SN location is  $0''.4$  east and  $27''.2$  north of the center of the galaxy UGC 7020 at a redshift of 0.020454 (Zhang et al. 2019). SN 2019uo was classified on 2019 January 19.9

UT as a SN II (Zhang et al. 2019) with the spectrum obtained with the Yunnan Faint Object Spectrograph and Camera (YFOSC) mounted on the 2.4 m LiJiang Telescope (LJT) at Yunnan Observatory (YNAO). Zhang et al. (2019) reported that the spectrum depicted a blue continuum and highly ionized “flash features” such as N V, He II and O V. However, this classification of type II SN was modified later by Fremling et al. (2019) and SN 2019uo was classified as a type Ibn. Prominent narrow emission lines of He I in the initial spectra of SN 2019uo indicating a P-cygni velocity of  $650\text{ km s}^{-1}$  justified the type Ibn classification. SN 2019uo is the second SN Ibn to show these features after SN 2010al. Adopting  $H_0 = 73\text{ km s}^{-1}\text{ Mpc}^{-1}$ , we obtain a luminosity distance of 88.8 Mpc for SN 2019uo. The Milky Way extinction along the line of sight of SN 2019uo is  $A_V = 0.035\text{ mag}$  (Schlafly & Finkbeiner 2011). For estimating the extinction along the line of sight within host galaxy, we estimate equivalent widths of the Na ID line in the first three spectra of SN 2019uo. Using the formulation by Munari & Zwitter (1997) and Poznanski et al. (2012), we estimate  $A_V = 0.2517\text{ mag}$ . This estimate also brings the  $B - V$  colors of SN 2019uo into close agreement with SNe 2006jc and 2010al. Thus, we adopt a total  $A_V = 0.287\text{ mag}$ . The temporal and spectral evolution of SN 2019uo and the detailed modeling of the bolometric light curve is discussed in the sections to follow.

## 2. DATA ACQUISITION AND REDUCTION

We observed SN 2019uo with Las Cumbres Observatory (LCO) in the *UBVgri* filters from  $\sim 2$  to 106 days after discovery. Augmenting the LCO data, photometric observations in *UBVRI/ugri* were also taken with 0.7m BITRAN-CCD Imaging System located in Japan; 0.8m Tsinghua-NAOC Telescope (TNT), Xinglong Observatory, China; 1.04m Sampurnanand Telescope (ST); 1.30m Devasthal Fast Optical Telescope (DFOT), ARIES, India; 2.00m Himalayan Chandra Telescope (HCT), IAO, Hanle, India and Lijiang 2.4m Telescope (LJT), Yunnan Observatories (YNAO), China. We performed image subtraction using High Order Transform of PSF AND Template Subtraction (HOTPANTS)<sup>1</sup>(Becker 2015). The instrumental magnitudes were estimated using IRAF<sup>2</sup>(Tody 1986, 1993) and DAOPHOT<sup>3</sup>(Stetson 1987). The LCO photometry was done using *lcogetsnpipe*<sup>4</sup> (see Valenti et al. 2011,

<sup>1</sup> <https://github.com/acbecker/hotpants>

<sup>2</sup> Image Reduction and Analysis Facility

<sup>3</sup> Dominion Astrophysical Observatory Photometry

<sup>4</sup> <https://github.com/svalenti/lcogetsnpipe>

**Table 1.** Photometry of SN 2019uo

Date (yyyy-mm-dd)	JD (2458000+)	Phase <sup>†</sup> (day)	<i>U</i> (mag)	<i>B</i> (mag)	<i>g</i> (mag)	<i>V</i> (mag)	<i>r</i> (mag)	<i>i</i> (mag)	Telescope
2019-01-18	501.8	-6.8	—	17.865±0.107	17.637±0.097	17.927±0.146	17.936±0.139	—	LCO
2019-01-20	503.9	-4.7	16.452±0.033	16.937±0.027	16.785±0.013	17.052±0.026	17.039±0.019	17.353±0.033	LCO
2019-01-20	504.3	-4.3	—	16.817±0.052	16.908±0.162	17.262±0.050	—	17.423±0.052	TNT
2019-01-21	505.3	-3.3	—	16.623±0.013	16.768±0.018	17.014±0.030	16.901±0.029	17.328±0.038	TNT
2019-01-21	505.2	-3.4	—	—	—	16.882±0.08	—	—	0.7m
2019-01-22	506.2	-2.4	—	—	—	16.777±0.063	—	—	0.7m
2019-01-23	506.8	-1.8	16.122±0.074	—	16.613±0.039	16.883±0.051	—	—	LCO
2019-01-23	507.3	-1.3	—	16.654±0.036	16.699±0.022	16.991±0.034	16.821±0.034	17.187±0.042	LCO
2019-01-24	507.8	-0.8	16.252±0.075	16.731±0.031	16.532±0.015	16.669±0.027	16.676±0.022	17.215±0.022	LCO
2019-01-25	508.1	-0.6	—	—	—	16.673±0.024	—	17.037±0.015	LJT
2019-01-25	508.3	-0.3	16.015±0.020	16.825±0.031	16.655±0.019	16.616±0.101	16.782±0.022	17.027±0.0272	LJT, TNT, 0.7m
2019-01-25	508.8	0.1	16.199±0.051	16.740±0.026	16.565±0.017	16.685±0.028	16.654±0.023	17.003±0.055	LCO
2019-01-28	511.4	2.7	—	—	—	16.732±0.143	—	—	0.7m
2019-01-28	511.8	3.1	16.331±0.028	17.156±0.017	—	16.749±0.0153	16.646±0.010	—	DFOT
2019-01-30	513.1	4.5	—	—	—	16.786±0.085	—	—	ST
2019-02-01	515.7	7.1	17.334±0.049	17.447±0.026	17.281±0.009	17.307±0.019	17.237±0.011	17.430±0.021	LCO
2019-02-02	516.3	7.6	—	17.547±0.016	17.257±0.011	17.655±0.022	17.532±0.016	17.696±0.013	TNT
2019-02-04	518.4	9.8	—	18.275±0.016	—	—	17.847±0.017	17.948±0.014	ST
2019-02-04	518.8	10.2	18.262±0.082	18.276±0.029	17.921±0.016	17.882±0.025	17.835±0.021	17.938±0.030	LCO
2019-02-05	519.2	10.5	—	18.754±0.031	—	17.885±0.024	17.856±0.017	—	ST
2019-02-06	520.3	11.7	—	18.862±0.024	—	18.141±0.025	18.479±0.027	18.592±0.033	ST
2019-02-08	523.4	14.8	19.787±0.041	19.058±0.027	—	18.316±0.031	18.900±0.001	18.808±0.052	HCT
2019-02-09	524.4	15.7	—	19.224±0.069	—	18.598±0.029	18.911±0.037	19.091±0.033	ST
2019-02-12	527.0	18.4	—	19.487±0.053	19.169±0.037	18.946±0.043	19.012±0.048	19.136±0.075	LCO
2019-02-20	535.2	26.6	—	—	20.037±0.218	—	—	20.287±0.115	TNT
2019-02-21	536.2	27.6	—	—	20.228±0.214	—	—	—	TNT
2019-02-23	538.1	29.5	—	—	20.265±0.312	—	—	—	TNT
2019-03-02	544.3	36.2	—	21.231±0.274	20.726±0.138	20.526±0.178	21.032±0.305	21.096±0.215	LCO

<sup>†</sup> with respect to JD<sub>max</sub> = 2458508.65.

2016) on the difference images. The instrumental SN magnitudes were calibrated using the standard magnitudes of a number of local stars in the SN field obtained from the Sloan Digital Sky Survey (SDSS) catalog for the *gri* bands and the Landolt standard fields taken on the same night by the same instrument as the science images for *UBV*. Wherever required, the *RI* magnitudes were converted to *ri* using the equations of Jordi et al. (2006). The photometry of SN 2019uo is presented in Table 1.

The spectroscopic observations were taken at 9 epochs spanning up to  $\sim 88$  days after discovery. The 1D wavelength- and flux-calibrated spectra were extracted using the floydsspec pipeline (Valenti et al. 2014) for the LCO data. Spectroscopic data reduction of the 2.2 m and 2.4 m telescopes was done using the APALL task in IRAF followed by wavelength and flux calibration. The slit loss corrections were done by scaling the spectra to the photometry. Finally, the spectra were corrected for the heliocentric redshift of the host galaxy. The log of spectroscopic observations is given in Table 2.

### 3. PHOTOMETRIC EVOLUTION OF SN 2019UO

The complete multi-band light curve of SN 2019uo is shown in Figure 1. With our available observations, we were able to trace the epoch of maximum in all

the bands. The date of maximum and its brightness were determined by fitting a cubic spline to the *UB-Vgri* light curves. The maximum in *r*-band occurred on JD  $2458508.6 \pm 0.5$  at an apparent magnitude of  $16.66 \pm 0.03$  mag. The errors reported are obtained from interpolated measurements around the peak. We use days since *r*-maximum ( $r_{\text{max}}$ ) as a reference epoch throughout the paper. Assuming that the discovery date is close to explosion, we estimated a rise time of  $8.7 \pm 1.3$  days. This is similar to iPTF14aki and iPTF15akq (c.f. Table 4; Hosseinzadeh et al. 2017).

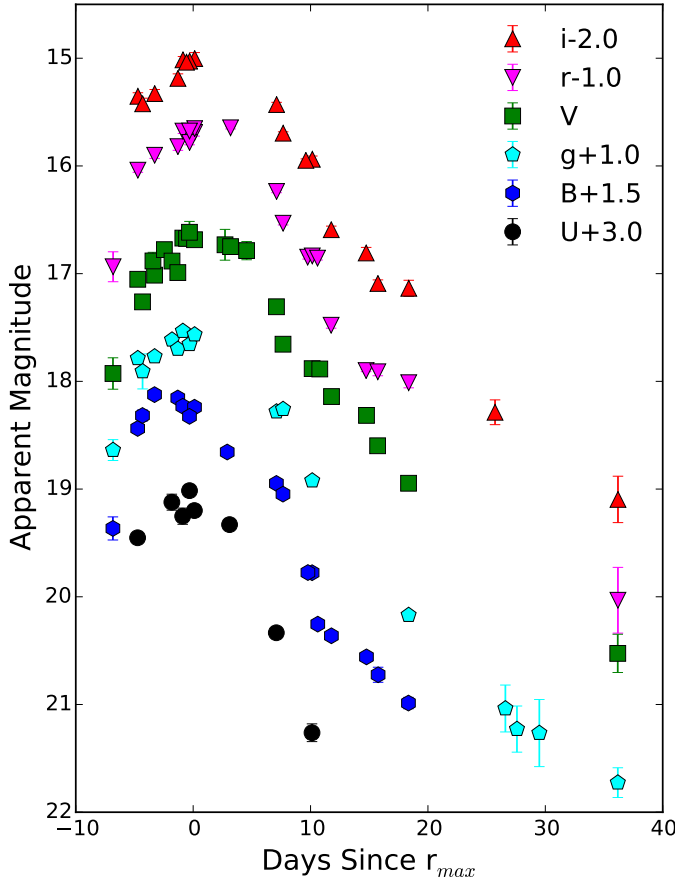
The *r*-band light curve, between 0–36 days, decays with a rate of  $0.126 \pm 0.005$  mag d<sup>-1</sup>. The *g*, *B*, *V* and *i* bands follow approximately the same decline rate. The sample of SNe Ibn in Hosseinzadeh et al. (2017) are fast-evolving with a typical decline rate of 0.1 mag d<sup>-1</sup> during the first month post-maximum. SN 2019uo follows the same decline rate.

Figure 2 shows the absolute magnitude light curve of SN 2019uo along with other SNe Ibn after correcting for distance and extinction. The peak *r*-band absolute magnitude of SN 2019uo is  $-18.30 \pm 0.24$  mag, which is at the fainter end of SN Ibn sample. The blue band in Figure 2 shows the average light curve (comprising of 95% of the SN Ibn data) of SNe Ibn taken from Hosseinzadeh et al. (2017). The average light curve was generated by using

**Table 2.** Log of spectroscopic observations of SN 2019uo.

Date	JD – 2458000	Phase <sup>†</sup>	Telescope	Instrument	Range (Å)
2019-01-19	503.4	-5.2	2.4 m LJT	YFOSC	3500-8800
2019-01-20	503.9	-4.7	2.0 m FTN	FLOYDS	3200-9000
2019-01-21	504.9	-3.7	2.0 m FTN	FLOYDS	3200-9000
2019-01-23	506.9	-1.7	2.0 m FTN	FLOYDS	3200-9000
2019-01-24	508.3	-0.3	2.4 m LJT	YFOSC	3500-8800
2019-01-28	512.4	3.8	2.0 m FTN	FLOYDS	3200-9000
2019-02-05	519.9	11.3	2.0 m FTN	FLOYDS	3200-9000
2019-02-08	523.8	15.2	2.2 m China	BFOSC	4000-10000
2019-02-14	529.2	20.6	2.4 m LJT	YFOSC	3500-8800

<sup>†</sup> with respect to JD<sub>max</sub> = 2458508.65.

**Figure 1.** *UBVgri* light curve evolution of SN 2019uo.

a Gaussian process to fit a smooth curve to the combined light curves on the sample of [Hosseinzadeh et al. \(2017\)](#). The fit was performed in log-log space to ensure consistency and smoothness between the early and late time light curves. The average light curve, thus, generated also uses the Gaussian process to fit positive and negative residuals. It is to note that SN 2019uo is  $\sim 1.2$  mag fainter than the normalized SNe Ibn light curve.

We compare the  $B - R/r$  color evolution of SN 2019uo with a number of type Ibn SNe, which usually show heterogeneity in their color evolution. The  $B - r$  color of SN 2019uo increases up to 0.64 mag  $\sim 20$  days post  $r_{max}$ , subsequently becoming blue at  $\sim 36$  days. Similarly, for SN 2010al and iPTF14aki the  $B - r$  color increases up to  $\sim 1$  mag,  $\sim 30$  days post  $R_{max}$ . Thus, SN 2019uo shows a color evolution similar to SN 2010al and iPTF14aki. At similar epochs, the color evolution of SN 2006jc was extremely blue ( $-0.5$  mag). SN 2006jc, then shows an overall flatter color evolution. The early blue colour are typical of type Ibn SN ([Pastorello et al. 2016](#)). The transition to redder colours for SNe 2019uo and 2010al places their behavior between SNe Ib and most extreme SNe Ibn. SN 2006jc ([Pastorello et al. 2007](#)) and OGLE-2012-SN-006 ([Pastorello et al. 2015a](#)) show redder colours post 50 days.

#### 4. SPECTRAL EVOLUTION

The spectral evolution of SN 2019uo from  $-5.2$  days to 20.6 days post maximum is displayed in Figure 3.

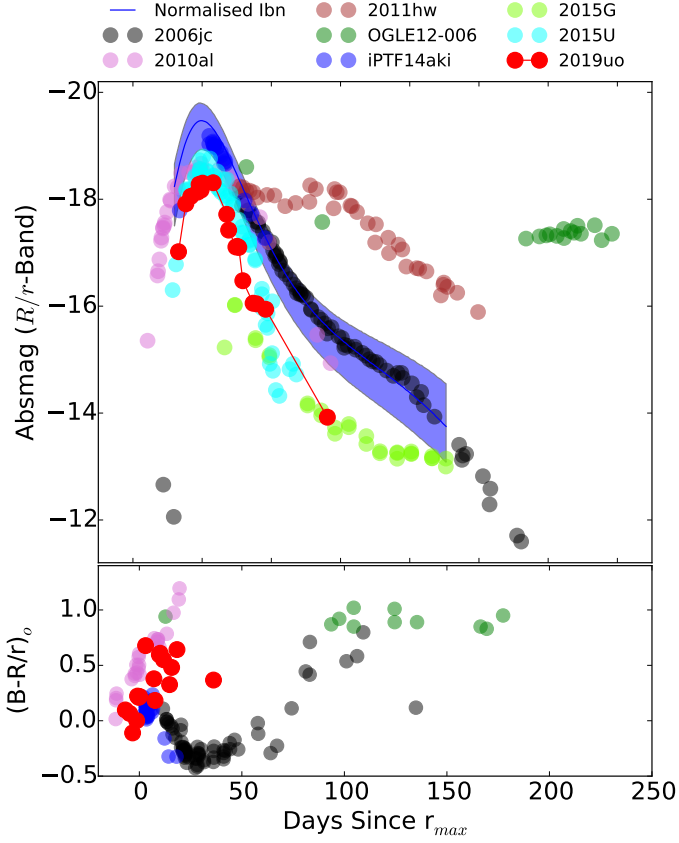


**Figure 2.**  $R/r$ -band absolute magnitude light curve and  $B - R/r$  colour curve of SN 2019uo. The comparison sample includes SNe 2006jc (Pastorello et al. 2007; Foley et al. 2007), 2010al (Pastorello et al. 2015b), OGLE-SN-006 (Pastorello et al. 2015a), 2011hw (Pastorello et al. 2015b), iPTF14aki (Hosseinizadeh et al. 2017), 2015U (Shivvers et al. 2016; Hosseinizadeh et al. 2017) and 2015G (Hosseinizadeh et al. 2017).

The early spectral sequence shows a unique blue continuum similar to SN 2010al. Blackbody fits to the first three spectra ( $-5.2$ ,  $-4.7$ , and  $-3.7$  days) show that the photospheric temperature varies between 13,000 K and 10,000 K. A very narrow H emission line ( $\leq 137$  km s $^{-1}$ ; unresolved) in the early spectrum of SN 2019uo is most likely due to interstellar gas in the host galaxy. Prominent emission features in the first three spectra ( $-5.2$  to  $-3.7$  days) of SN 2019uo are seen around  $\sim 4660$  Å. The emission components are double-peaked, with the blue component peaking at 4643 Å and the red component peaking at 4682 Å. The red component at 4682 Å is due to He II at 4686 Å, whereas the blue component arises from a blend of C III 4648 Å and N III 4640 Å. Another interesting feature is the possible identification of a doubly ionized C III feature at 5696 Å. Pastorello et al. (2015c) interpreted these as flash ionization signatures in a He-rich CSM (also see Gal-Yam

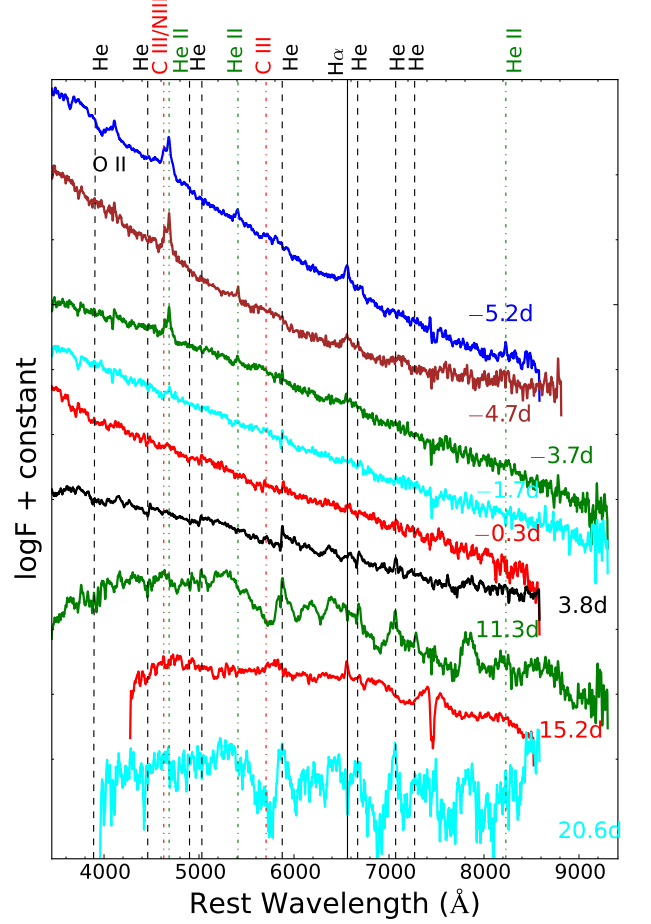


**Figure 3.** Spectral evolution of SN 2019uo from  $-5.2$  days to 20 days post  $r_{max}$ . Prominent He features are seen in the early spectra. Flash ionization signatures of He II, C III and N III are also seen.

2014). Although C III features were found in PTF12ldy and iPTF15ul (Hosseinizadeh et al. 2017), SN 2010al is the only previous SN Ibn where flash ionization signatures of C III and He II, typical of SNe II, are both seen. Cooke et al. (2010) and Silverman et al. (2010) identified such lines to be originating from a WR wind, previously noted in SNe IIn (e.g., SN 1998S; Fassia et al. (2001) and SN 2008fq; Taddia et al. (2013)). We also identify a He II 5411 Å feature with a velocity of 1483 km s $^{-1}$  at  $-5.2$  days. In the spectrum at  $-5.2$  days, we see a deep absorption feature at  $\sim 4000$  Å and a small dip around 8200 Å, which is likely due to the presence of O II and He II features, respectively.

Figure 4 shows the spectra of SNe 1998S (type IIn) and 2010al (type Ibn) in comparison with SN 2019uo. These two SNe have previously shown flash ionization signatures. While the spectrum of SN 2010al shows C III features around 4650 Å only, SN 2019uo shows C III





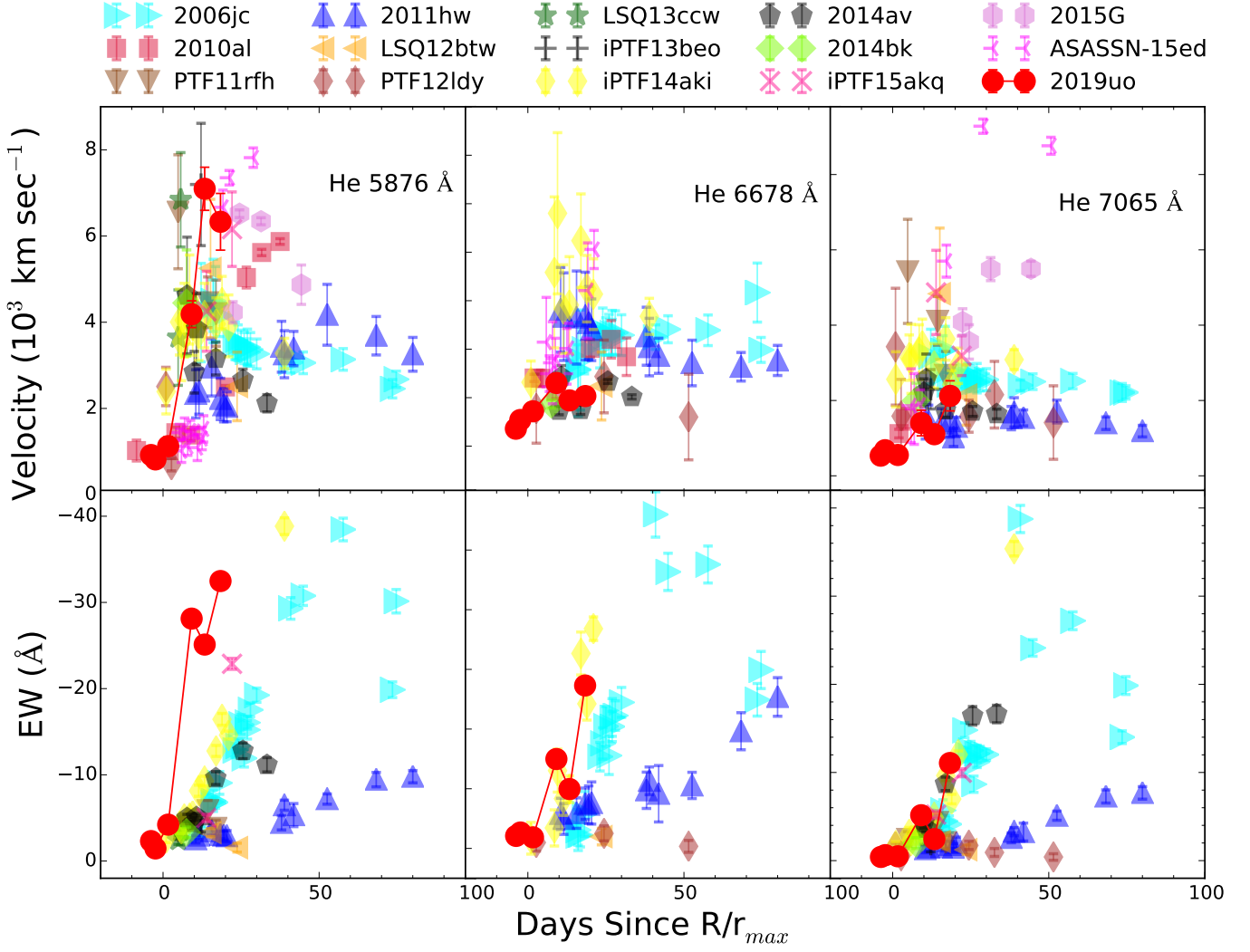


**Figure 6.** Evolution of line velocities and equivalent widths of He I emission lines is shown in top and bottom panels, respectively. The data for this are taken from — SNe 2006jc (Foley et al. 2007; Pastorello et al. 2008), 2010al (Pastorello et al. 2015c), 2011hw (Pastorello et al. 2015c), PTF11rfh (Hosseinizadeh et al. 2017), LSQ12btw (Pastorello et al. 2015b), OGLE12-006 (Pastorello et al. 2015a), PTF12ldy (Hosseinizadeh et al. 2017), iPTF13beo (Gorbikov et al. 2014), LSQ13ccw (Pastorello et al. 2015b), iPTF14aki (Hosseinizadeh et al. 2017), 2014av (Pastorello et al. 2016), 2014bk (Pastorello et al. 2016), iPTF15akq (Hosseinizadeh et al. 2017), ASASSN-15ed (Pastorello et al. 2015d), and 2015G (Hosseinizadeh et al. 2017).

ature and optical depths. Karamehmetoglu et al. (2019) suggest that dominance of emission at late phases is not because of being optically thin, but because they lack other lines to branch into it. He ionisation and recombination are mostly caused by UV and X-ray, occurring at shock boundary, deep in interacting regions. Even though most of the emission and the electron scattering are produced by the ionised region outside the shock, P-cygni features usually originate from optical depths  $\leq 1$ . X-rays penetrating further into the P-cygni producing regions will fill in the absorption and lead to emission features. Thus, this provides an alternative scenario to

the transitioning of P-cygni to emission features of He I lines for type I<sub>bn</sub> SNe.

The measured the expansion velocities and equivalent widths (EWs) of three neutral He lines (5876, 6678, and 7065 Å), wherever visible. We fit the emission lines of He I using a Gaussian on a linear continuum. The EW is estimated through the integral of the flux normalized to the local continuum. We do not measure the EW of the P-cygni lines. The velocities reported are estimated from the absorption minima of P-cygni profiles. Figure 6 shows the evolution of velocity and EW for a sample of SNe I<sub>bn</sub> taken from Hosseinizadeh et al. (2017) with time. We see that both the line velocities and EW of the

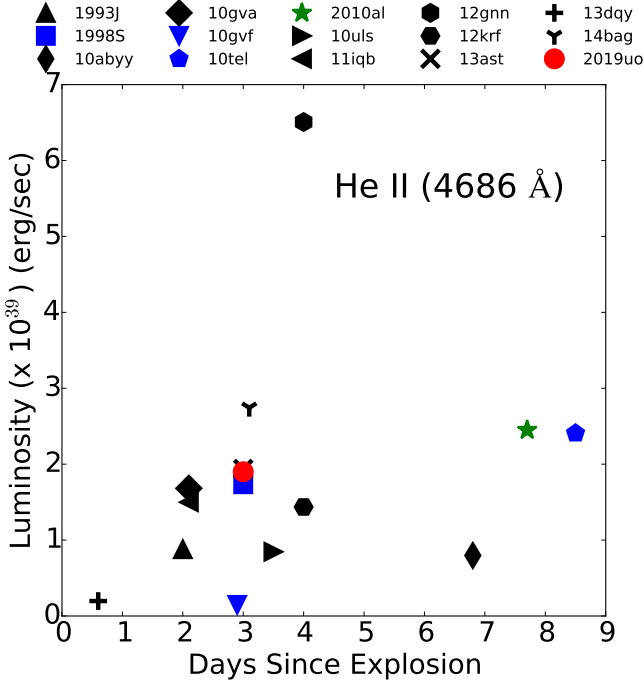


**Figure 7.** He II luminosity of a sample of SNe II, IIn, and Ibn (Khazov et al. 2016) with flash ionization signatures. Blue symbols: type IIn, Black symbols: type II (IIf, IIP and IIL), Red symbols: type Ibn.

He lines gradually increase with time and the velocity estimates of SN 2019uo lie in the lower range of SNe Ibn. However, SN 2019uo shows a faster evolution in line velocities, reaching broader emission profiles as seen in the P-cygni subclass (Hosseinzadeh et al. 2017) while the emission subclass shows very little velocity evolution.

To ascertain the origin of the SNe Ibn, we collected a sample of 12 SNe II (including SNe IIf and IIP, IIn) and Ibn from Khazov et al. (2016) that showed signatures of flash ionization within 10 days of explosion. Since the H lines are usually contaminated by the host galaxy, we selected the relatively unblended He II 4686 Å line. Since the He II lines are much narrower than lines from the SN ejecta, they can serve as a good tool for probing the flash-ionized CSM. When measuring the luminosities, we removed the continuum by fitting a linear function. Figure 7 shows that the typical luminosity of the He II line for SN 2019uo is similar to the type IIn SNe 1998S and PTF13ast.

## 5. MODELING THE BOLOMETRIC LIGHT CURVE OF SN 2019UO

To construct the bolometric light curve of SN 2019uo, the measured flux values were corrected for distance and reddening as given in Section 1. Spectral energy distributions (SEDs) were constructed accounting for the

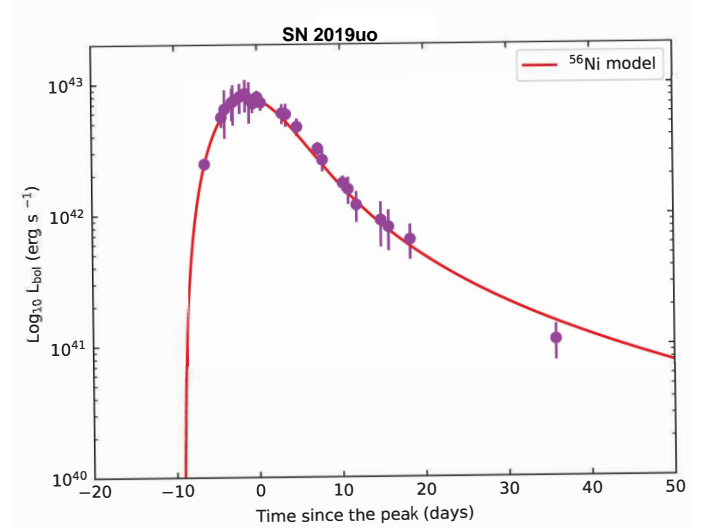


**Figure 8.** Best-fit light curves of SN 2019uo using a  $^{56}\text{Ni}$  model.

flux coverage between UV to IR bands using the *SuperBol* (Nicholl 2018) code. The lack of UV and NIR data was supplemented by extrapolating the SEDs using the blackbody approximation and direct integration method as described in Lusk & Baron (2017). A linear extrapolation was performed in UV regime at late times. The estimated peak bolometric luminosity of SN 2019uo is  $8.9 \times 10^{42} \text{ erg s}^{-1}$ . We used different models to fit the bolometric light curve at a fixed optical opacity of  $0.1 \text{ cm}^2 \text{ g}^{-1}$ . A Markov Chain Monte Carlo (MCMC) technique was used to obtain the best-fit parameters.

**$^{56}\text{Ni}$  model:** Assuming that the peak bolometric luminosity is powered by the decay of  $^{56}\text{Ni}$  to  $^{56}\text{Co}$ , we fit the bolometric light curve using  $^{56}\text{Ni}$  model (Arnett 1982, 1980). The parameters of the  $^{56}\text{Ni}$  model are the ejecta mass  $M_{\text{ej}}$ , the initial scale velocity of the ejecta  $v_{\text{sc0}}$ , the  $^{56}\text{Ni}$  mass  $M_{\text{Ni}}$ , the gamma-ray opacity of  $^{56}\text{Ni}$  decay photons  $\kappa_{\gamma, \text{Ni}}$  and explosion time  $t_{\text{expl}}$ . The initial kinetic energy of the ejecta is neutrino-driven and is considered to be  $E_k = 0.3 M_{\text{ej}} v_{\text{sc0}}^2$ . The best-fit parameters are tabulated in Table 3 and the best-fit model is displayed Fig. 8. The corner plot showing the covariance of the estimated parameters are represented in Fig. 9. We note that the  $^{56}\text{Ni}$  mass obtained from the powering mechanism of Arnett (1982) are in concordance with the values quoted for several stripped envelope SNe (Lyman et al. 2016; Prentice et al. 2016, 2019). Although the  $^{56}\text{Ni}$  mass inferred from the model is  $\sim 0.24 M_{\odot}$  which is comparable to that of normal CCSNe, the opacity for the gamma ray  $\kappa_{\gamma, \text{Ni}}$  emitted from the cascade decay of  $^{56}\text{Ni}$  is  $0.01 \text{ cm}^2 \text{ g}^{-1}$ , which is significantly smaller than the canonical lower limit which is  $0.025\text{--}0.027 \text{ cm}^2 \text{ g}^{-1}$ .



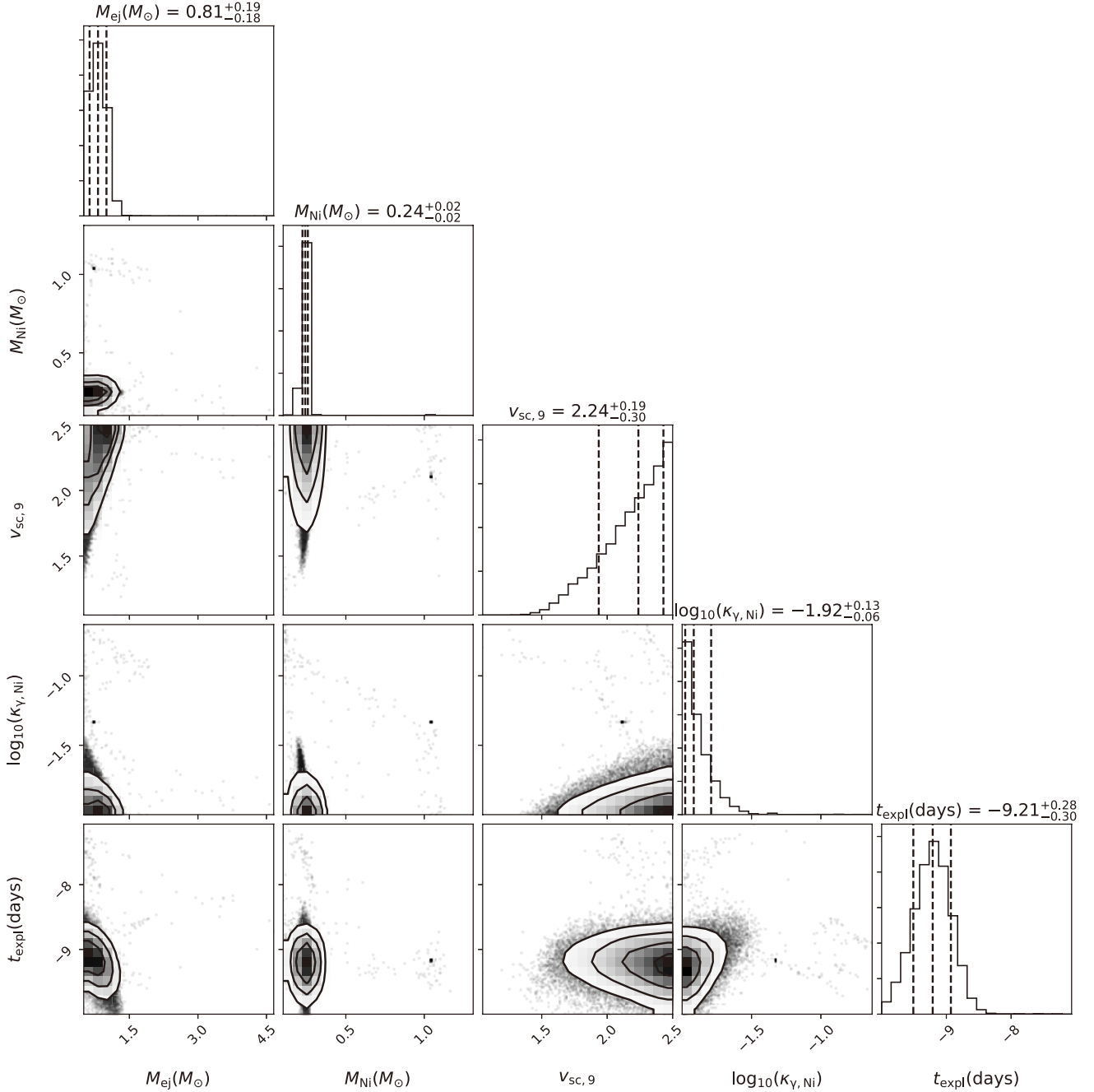


**Figure 9.** The corner plot of the  $^{56}\text{Ni}$  model displaying covariance of estimated parameters.

Therefore, the  $^{56}\text{Ni}$  model is not a good model in explaining the light curve of SN 2019uo and other models must be employed.

**The CSI model and the  $^{56}\text{Ni}$  + CSI model:** The narrow He emission lines appearing in the spectra of SN 2019uo indicate a potential source of circumstellar interaction (CSI) with a nearby He-rich shell. Thus, the nearby He-rich wind or shell surrounding the progeni-

tor could be the essential powering source of the bolometric light curve of SN 2019uo. We take into account the ejecta-CSM interaction model (i.e., the CSI model) (Chevalier 1982; Chevalier & Fransson 1994; Chugai & Danziger 1994; Ginzburg & Balberg 2012; Liu et al. 2018) and the  $^{56}\text{Ni}$  + CSI model (Chatzopoulos et al. 2012). To fit the bolometric light curve of SN 2019uo, we adopt the formulation given in Wang & Li (2019).

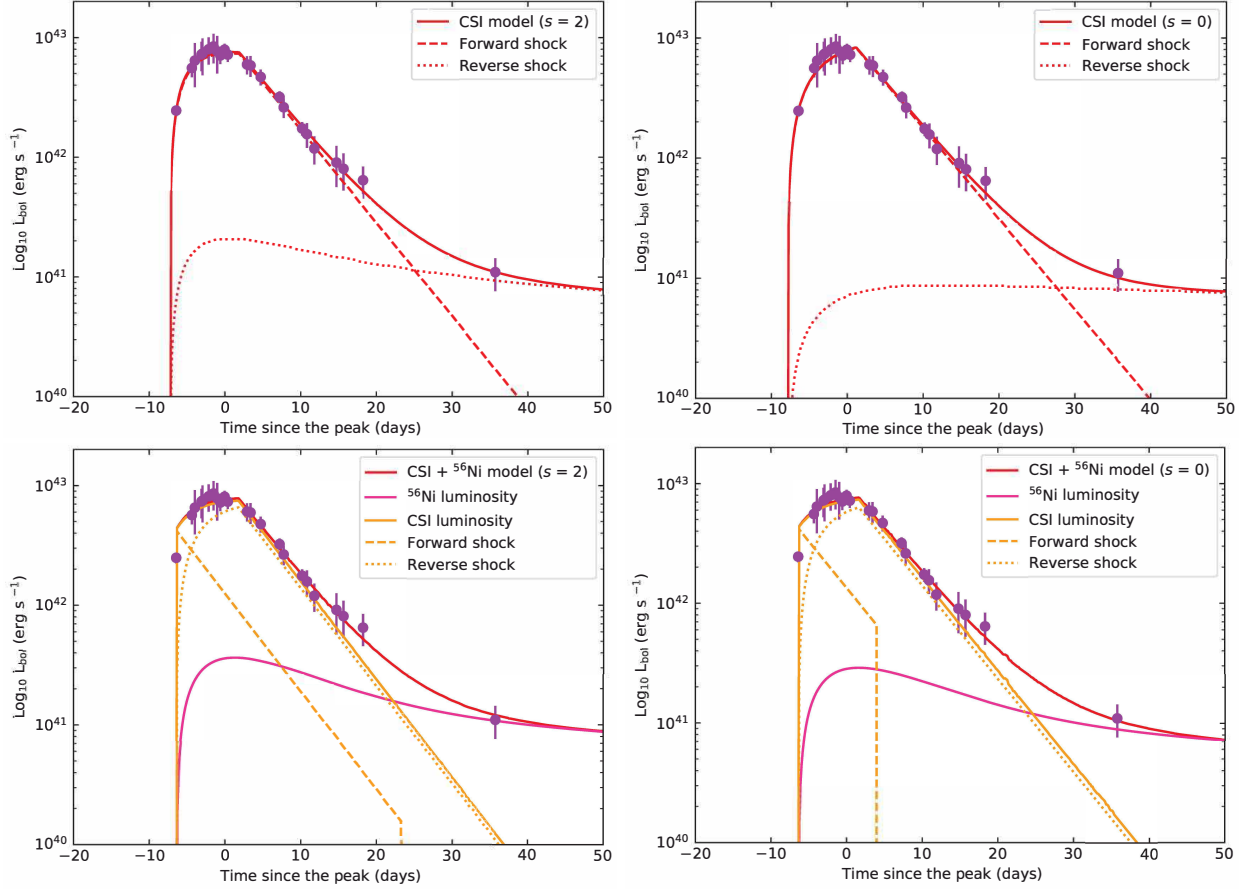


**Figure 10.** Best-fit light curves of SN 2019uo fitted with a CSI model and a combination of  $^{56}\text{Ni}$  and CSI. The forward shocks, reverse shocks, and  $^{56}\text{Ni}$  models are plotted with different lines.

**Table 3.** Parameters of the  $^{56}\text{Ni}$  model. The uncertainties are  $1\sigma$ .

$M_{\text{ej}}$ ( $M_{\odot}$ )	$M_{\text{Ni}}$ ( $M_{\odot}$ )	$v_{\text{sc0}}$ ( $10^9 \text{ cm s}^{-1}$ )	$\kappa_{\gamma, \text{Ni}}$ ( $\text{cm}^2 \text{ g}^{-1}$ )	$t_{\text{expl}}^*$ (days)	$\chi^2/\text{dof}$
$0.81^{+0.19}_{-0.18}$	$0.24^{+0.02}_{-0.02}$	$2.24^{+0.19}_{-0.30}$	$0.01^{+0.00}_{-0.00}$	$-9.21^{+0.28}_{-0.30}$	6.67/19

★ The value of  $t_{\text{expl}}$  is with respect to  $r_{\text{max}}$ .

The ejecta can be broadly distinguished into two zones, the inner part ( $\rho_{\text{ej}} \propto r^{-\delta}$ ) and the outer part ( $\rho_{\text{ej}} \propto r^{-n}$ ). The density profile of the CSM can typically be described as a power law where  $\rho_{\text{CSM}} \propto r^{-s}$ , where  $s = 0$  corresponds to shells of the CSM and  $s = 2$  corresponds to winds. Assuming  $\delta = 1$  and  $n = 10$ , the adopted parameters of the CSM model are the energy of the SN ( $E_{\text{SN}}$ ), the mass of the ejecta ( $M_{\text{ej}}$ ), the mass of the CSM ( $M_{\text{CSM}}$ ), the density of the innermost part of the CSM  $\rho_{\text{CSM, in}}$ , the radius of the innermost part of the ejecta  $R_{\text{CSM, in}}$ , the efficiency factor which con-

verts kinetic energy to radiation ( $\epsilon$ ), the dimensionless  $x_0$  parameter<sup>5</sup>, and  $t_{\text{expl}}$ . Two additional parameters are used in the  $^{56}\text{Ni}$  + CSI model,  $M_{\text{Ni}}$  and  $\kappa_{\gamma, \text{Ni}}$ . The best-fit parameters of the model are tabulated in Table 4 and the best-fit models are displayed in Fig. 10. The corner plots describing covariance of the parameters are shown in Fig. 11, Fig. 12, Fig. 13 and Fig. 14 respectively. The tabulated values of ejecta masses of the four models are reasonable if the progenitor is a WR star of mass  $\sim 25 M_{\odot}$  and the metallicity is nearly solar (Crowther & Smartt 2007). We adopted the  $^{56}\text{Ni}$ , CSI model, and the  $^{56}\text{Ni}$  + CSI models to fit the bolometric light curve of SN 2019uo. The  $^{56}\text{Ni}$  model provides a favourable fit to the light curve, but this model cannot explain the He I emission lines present in the spectrum of SN 2019uo. These lines are likely generated because of the CSI. We therefore invoke CSI as the more favourable model to model light curve. For the

<sup>5</sup>  $x \equiv \frac{r(t)}{R(t)}$ , where  $x \leq x_0$  and  $x \geq x_0$  are inner and outer parts of the ejecta.

**Table 4.** Parameters of the CSI model and the CSI plus  $^{56}\text{Ni}$  model. The uncertainties are  $1\sigma$ .

	$s$	$E_{\text{SN}}$	$M_{\text{ej}}$	$M_{\text{Ni}}$	$M_{\text{CSM}}$	$\rho_{\text{CSM,in}}$	$R_{\text{CSM,in}}$	$\epsilon$	$x_0$	$\kappa_{\gamma,\text{Ni}}$	$t_{\text{expl}}^*$	$\chi^2/\text{dof}$
		( $10^{51}$ erg)	( $M_{\odot}$ )	( $M_{\odot}$ )	( $M_{\odot}$ )	( $10^{-12}$ g cm $^{-3}$ )	( $10^{14}$ cm)			(cm $^2$ g $^{-1}$ )	(days)	
CSI	2	$0.87^{+0.06}_{-0.04}$	$8.83^{+0.71}_{-0.99}$	...	$0.40^{+0.04}_{-0.03}$	$3.34^{+3.33}_{-1.72}$	$1.76^{+0.91}_{-0.55}$	$0.11^{+0.01}_{-0.01}$	$0.35^{+0.08}_{-0.10}$	...	$-7.24^{+0.09}_{-0.08}$	3.95/16
CSI	0	$0.40^{+0.31}_{-0.14}$	$13.51^{+3.91}_{-5.19}$	...	$1.28^{+0.41}_{-0.44}$	$0.15^{+0.12}_{-0.04}$	$19.05^{+6.66}_{-7.98}$	$0.51^{+0.29}_{-0.25}$	$0.67^{+0.20}_{-0.22}$	...	$-7.89^{+0.07}_{-0.07}$	13.44/16
CSI+ $^{56}\text{Ni}$	2	$1.67^{+0.18}_{-0.23}$	$15.99^{+2.25}_{-2.98}$	$0.01^{+0.003}_{-0.002}$	$0.41^{+0.08}_{-0.07}$	$20.96^{+4.73}_{-4.83}$	$8.04^{+1.49}_{-1.39}$	$0.64^{+0.14}_{-0.12}$	$0.51^{+0.25}_{-0.19}$	$0.95^{+10.15}_{-0.88}$	$-6.42^{+0.00}_{-0.00}$	2.79/14
CSI+ $^{56}\text{Ni}$	0	$1.78^{+0.13}_{-0.19}$	$16.30^{+2.09}_{-2.72}$	$0.01^{+0.003}_{-0.002}$	$0.73^{+0.12}_{-0.11}$	$25.05^{+2.75}_{-3.58}$	$14.16^{+1.85}_{-2.00}$	$0.71^{+0.12}_{-0.12}$	$0.43^{+0.22}_{-0.14}$	$0.90^{+10.40}_{-0.82}$	$-6.40^{+0.00}_{-0.00}$	3.17/14

★ The value of  $t_{\text{expl}}$  is with respect to  $r_{\text{max}}$ .

CSI model, the estimated ejecta masses for  $s = 0$  and  $s = 2$  are  $8.83^{+0.71}_{-0.99} M_{\odot}$  and  $13.51^{+3.91}_{-5.19} M_{\odot}$  respectively. This model, however, did not take into account the role of  $^{56}\text{Ni}$ . Using the combination of both  $^{56}\text{Ni}$  + CSI, the estimated  $M_{\text{ej}}$  for  $s = 0$  and  $s = 2$  is  $15.99^{+2.25}_{-2.98} M_{\odot}$  and  $16.30^{+2.09}_{-2.72} M_{\odot}$ , respectively, which are consistent with a WR progenitor scenario. The mass-loss rate is given by  $\dot{M} = 4\pi v_w q$  (where  $q = \rho_{\text{CSM,in}} R_{\text{CSM,in}}^2$ ). The velocity of the wind  $v_w = 100\text{--}1000$  km s $^{-1}$  for WR systems. Considering the wind CSI model ( $s = 2$ ), we find that the estimated mass-loss rate lies between  $0.195\text{--}1.95 M_{\odot} \text{ yr}^{-1}$ , which is comparable with the values obtained for iPTF13z ( $0.1\text{--}2 M_{\odot} \text{ yr}^{-1}$ ; Nyholm et al. 2017) and PS15dpn ( $1\text{--}10 M_{\odot} \text{ yr}^{-1}$ ; Wang & Li 2019). Using the combination of  $^{56}\text{Ni}$  + CSI model ( $s = 2$ ), the estimated mass loss rate lies between  $25.5\text{--}255.4 M_{\odot} \text{ yr}^{-1}$  which is significantly higher than the value obtained for iPTF13z, PS15dpn, and this model can be excluded. Nevertheless, the  $^{56}\text{Ni}$ +CSM shell is reasonable.

For the CSM shell and the  $^{56}\text{Ni}$  + CSM shell model, the expelled shell mass prior to explosion are  $\sim 1.3 M_{\odot}$  and  $0.73 M_{\odot}$ , respectively. The radius of the inner shell for the  $^{56}\text{Ni}$  + CSI model, as seen from Table 4, is  $14 \times 10^{14}$  cm and the typical velocity of WR winds is between  $100$  and  $1000$  km s $^{-1}$  ( $10^{7-8}$  cm s $^{-1}$ ); so the time at which the shell is expelled prior to explosion is estimated to be between  $1.4 \times 10^6$  s and  $1.4 \times 10^7$  s, i.e., between 163.8 and 1638.8 days.

## 6. SUMMARY

In this paper, we present the photometric and spectral evolution of the type I<sub>bn</sub> SN 2019UO. The typical light curve decay rate of SNe I<sub>bn</sub> is  $\sim 0.1$  mag d $^{-1}$  in all bands which is in agreement with the decline rates of the SNe I<sub>bn</sub> discussed by Hosseinzadeh et al. (2017). The color evolution of SN 2019UO is similar to SN 2010al and iPTF14aki which places it between SNe Ib and SNe I<sub>bn</sub>.

This is in good agreement with the P Cygni spectroscopic features that transition from narrow to broad, indicating a He-rich circumstellar shell around the progenitor star along with optically thick CSM (Hosseinzadeh et al. 2017). The absolute magnitude ( $M_{\text{max}}^V = -18.30 \pm 0.24$  mag) indicates that SN 2019UO lies at the fainter end of the group. We fit the bolometric light curve of SN 2019UO with  $^{56}\text{Ni}$  model. However, the  $^{56}\text{Ni}$  model alone does not take into account the CSM interaction that is evident from the narrow emission lines in the spectra of SN 2019UO. Thus, we also fit the light curves with a CSI model and a  $^{56}\text{Ni}$  + CSI model. The  $^{56}\text{Ni}$  + CSI wind ( $s=2$ ) model can be excluded since an unrealistic value of mass loss rate ( $25.5\text{--}255.4 M_{\odot} \text{ yr}^{-1}$ ) is required and the  $^{56}\text{Ni}$  + CSI shell model is reasonable. The combination of  $^{56}\text{Ni}$  + CSI shell well fits our observed light curve, with ejecta masses consistent with a WR star. The spectroscopic features of SN 2019UO indicate that it is the second SNe I<sub>bn</sub> with flash ionization signatures. Prominent lines of He II, C III, and N III are detected in the spectra, similar to SN 2010al. SN 2019UO shows initial P Cygni He I features that broadens after 11 days post-maximum. This can originate from a He-rich shell around progenitor surrounded by dense CSM, or it may be due to viewing angle dependency. This is also validated by the equivalent widths of He I features. Alternatively, P-cygni spectroscopic features usually originate from optical depths  $\leq 1$ . As X-rays penetrate into the P-cygni producing regions absorptions are filled leading to subsequent emission features. The estimated line velocities are lower than the average SN I<sub>bn</sub>, but they show a faster evolution compared to the group of SNe that show prominent emission features from the beginning.

## ACKNOWLEDGMENTS

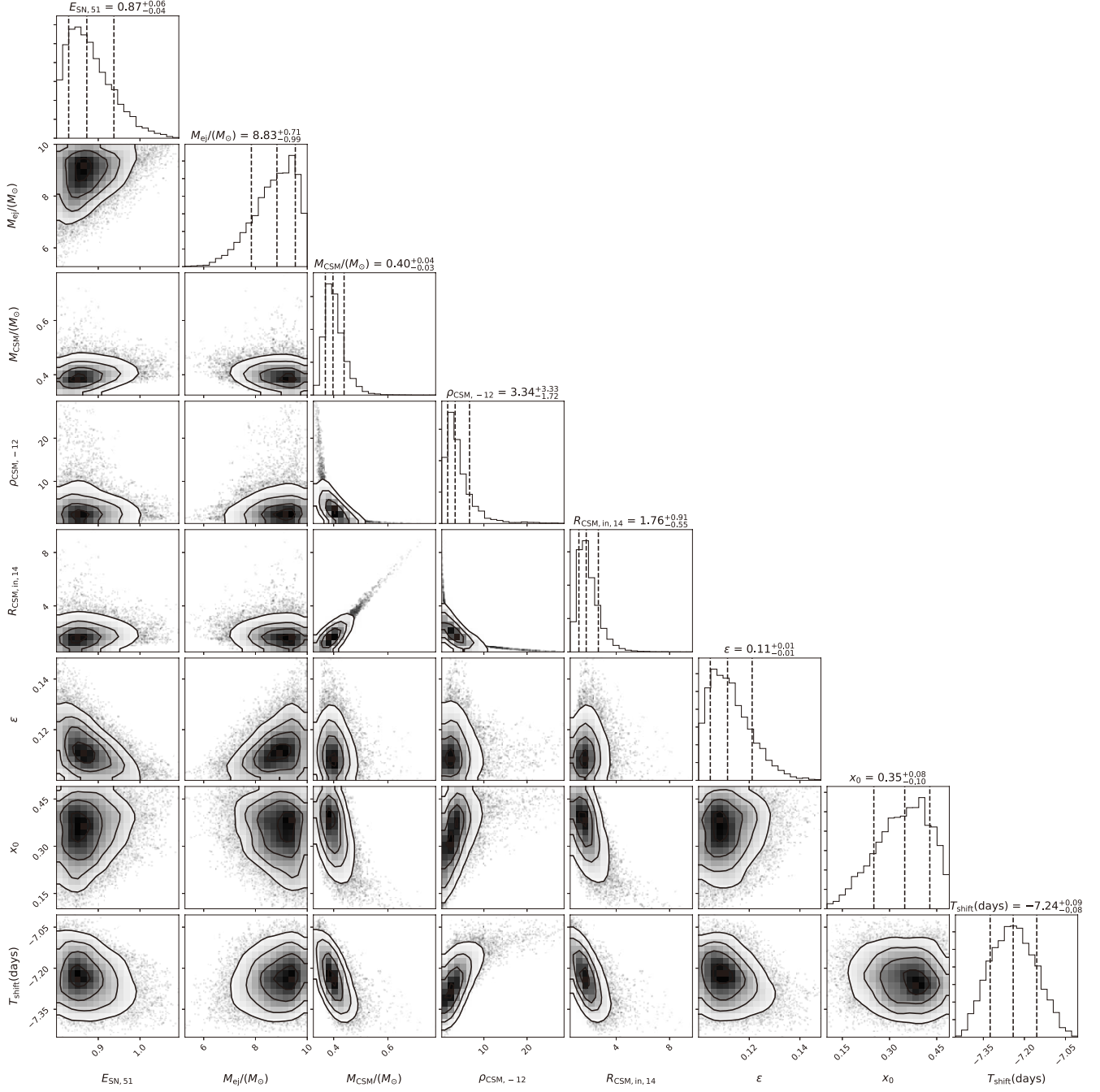


**Figure 11.** The corner plot of the CSI wind model displaying covariance of estimated parameters.

We thank the support of the staff of the Xinglong 2.16 m and Lijiang 2.4 m telescope, and observing assistants at the 1.04 m ST, 1.30 m DFOT, and 2.00 m HCT for their support during observations. This work was partially supported by the Open Project Program of the Key Laboratory of Optical Astronomy, National Astronomical Observatories, Chinese Academy of Sciences. Funding for the Lijiang 2.4 m telescope has

been provided by Chinese Academy of Sciences and the People's Government of Yunnan Province. We acknowledge Weizmann Interactive Supernova data REPOSITORY (WISereP; <http://wiserep.weizmann.ac.il>). DAH acknowledges support from NSF grant AST-1313404. The work of XW is supported supported by the National Natural Science Foundation of China (NSFC grants 11325313, 11633002, and 11761141001), and

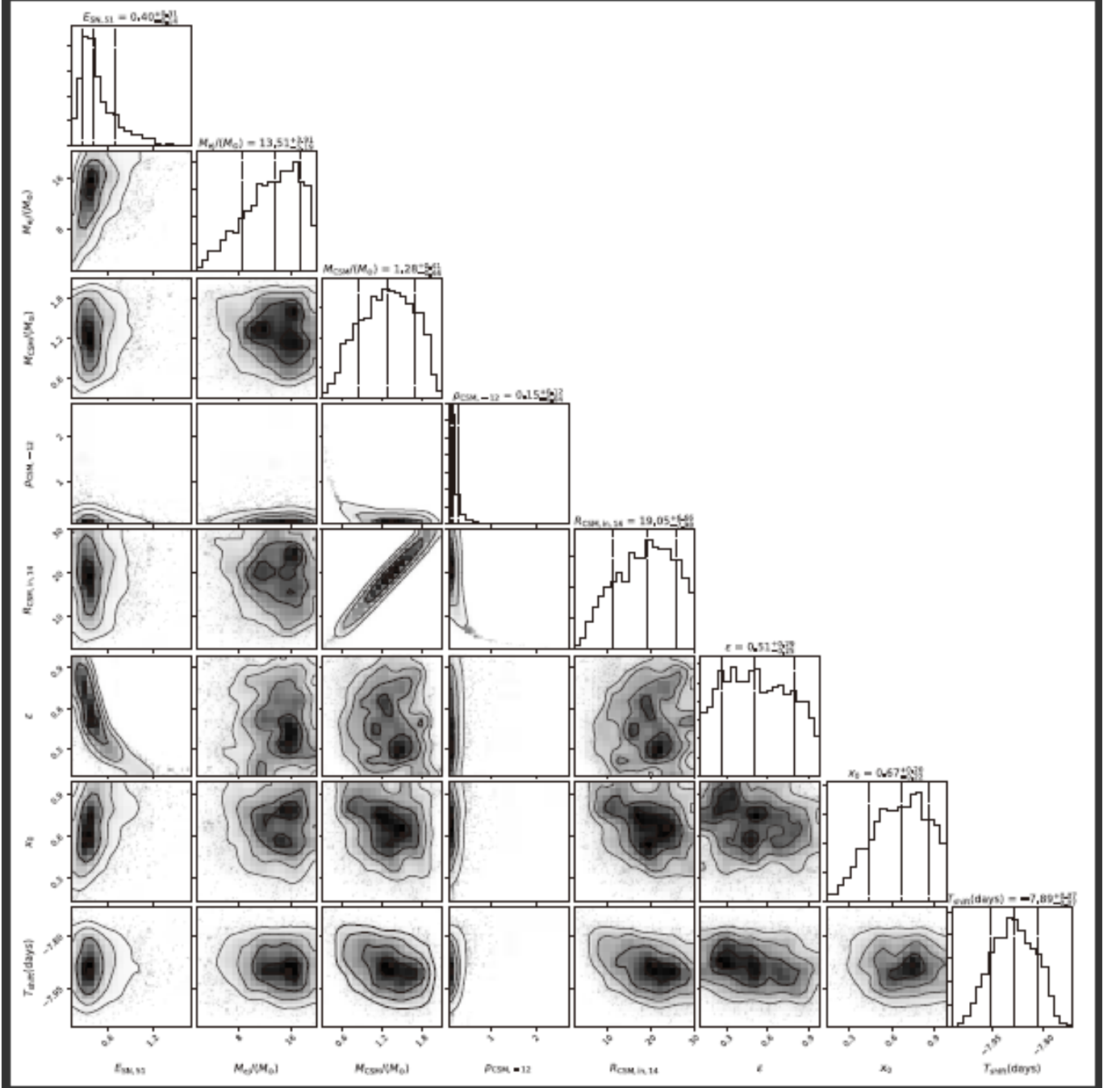


**Figure 12.** The corner plot of the CSI shell model displaying covariance of estimated parameters.

the National Program on Key Research and Development Project (grant no. 2016YFA0400803). This work makes use of data obtained with the LCO Network. KM and SBP acknowledges BRICS grant DST/IMRCD/BRICS/Pilotcall/ProFCheap/2017(G) for the present work. SBP and KM also acknowledge the DST/JSPS grant, DST/INT/JSPS/P/281/2018. KM acknowledges the support from Department of Science and Technology (DST), Govt. of India and

Indo-US Science and Technology Forum (IUSSTF) for the WISTEMM fellowship and Dept. of Physics, UC Davis where a part of this work was carried out. GCA, BK and DKS acknowledge BRICS grant DST/IMRCD/BRICS/PilotCall1/MuMeSTU/2017(G) for the present work. The work of SQW is supported by National Natural Science Foundation of China (Grants 11963001, 11533003, 11603006, 11673006, 11851304, and U1731239).



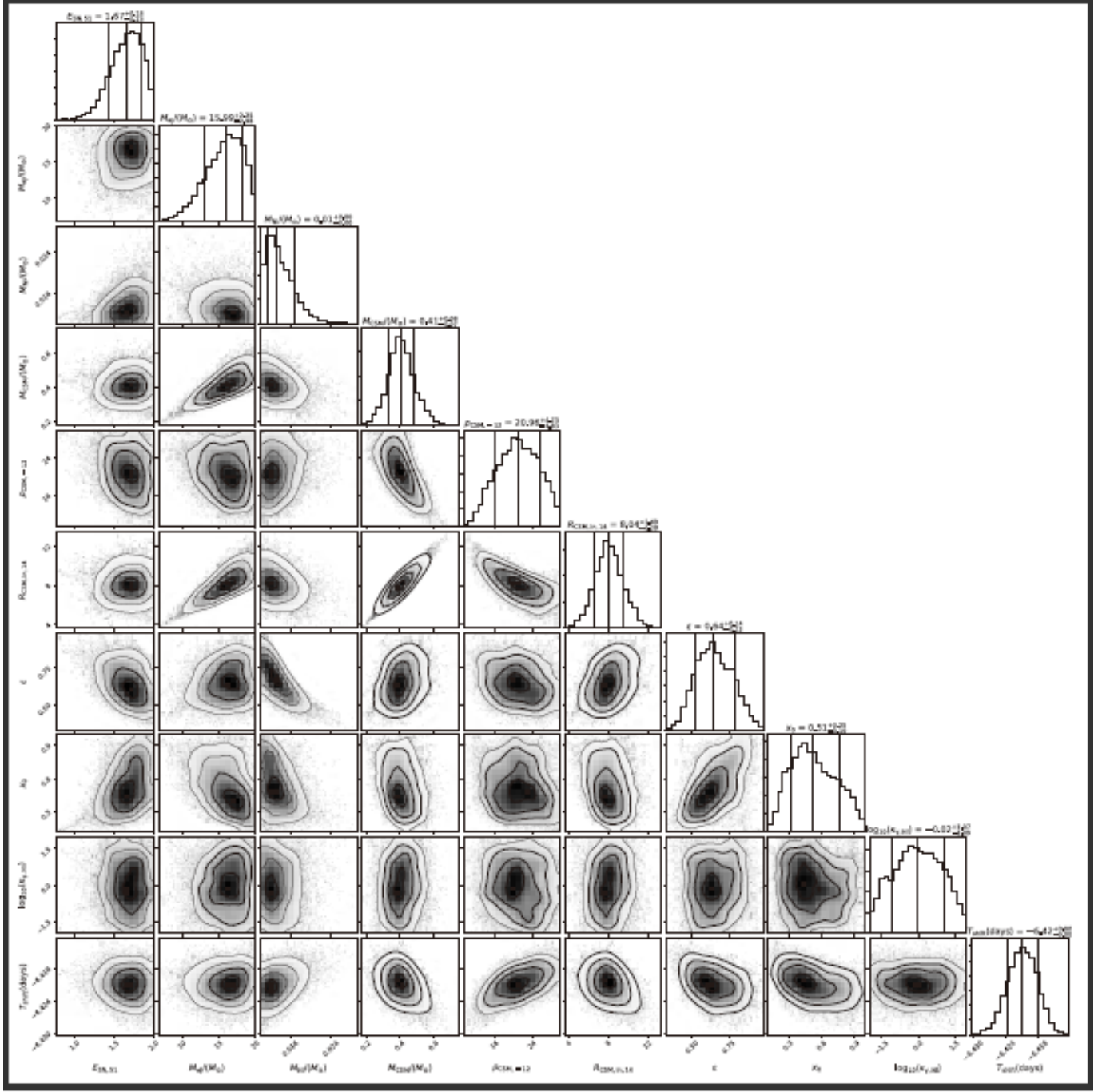


**Figure 13.** The corner plot of the  $^{56}\text{Ni}$  + CSI wind model displaying covariance of estimated parameters.

## REFERENCES

- Andrews, J. E., & Smith, N. 2018, MNRAS, 477, 74,  
doi: [10.1093/mnras/sty584](https://doi.org/10.1093/mnras/sty584)
- Arnett, W. D. 1980, ApJ, 237, 541, doi: [10.1086/157898](https://doi.org/10.1086/157898)
- . 1982, ApJ, 253, 785, doi: [10.1086/159681](https://doi.org/10.1086/159681)
- Becker, A. 2015, HOTPANTS: High Order Transform of PSF AND Template Subtraction.  
<http://ascl.net/1504.004>
- Chatzopoulos, E., Wheeler, J. C., & Vinko, J. 2012, ApJ, 746, 121, doi: [10.1088/0004-637X/746/2/121](https://doi.org/10.1088/0004-637X/746/2/121)
- Chevalier, R. A. 1982, ApJ, 258, 790, doi: [10.1086/160126](https://doi.org/10.1086/160126)

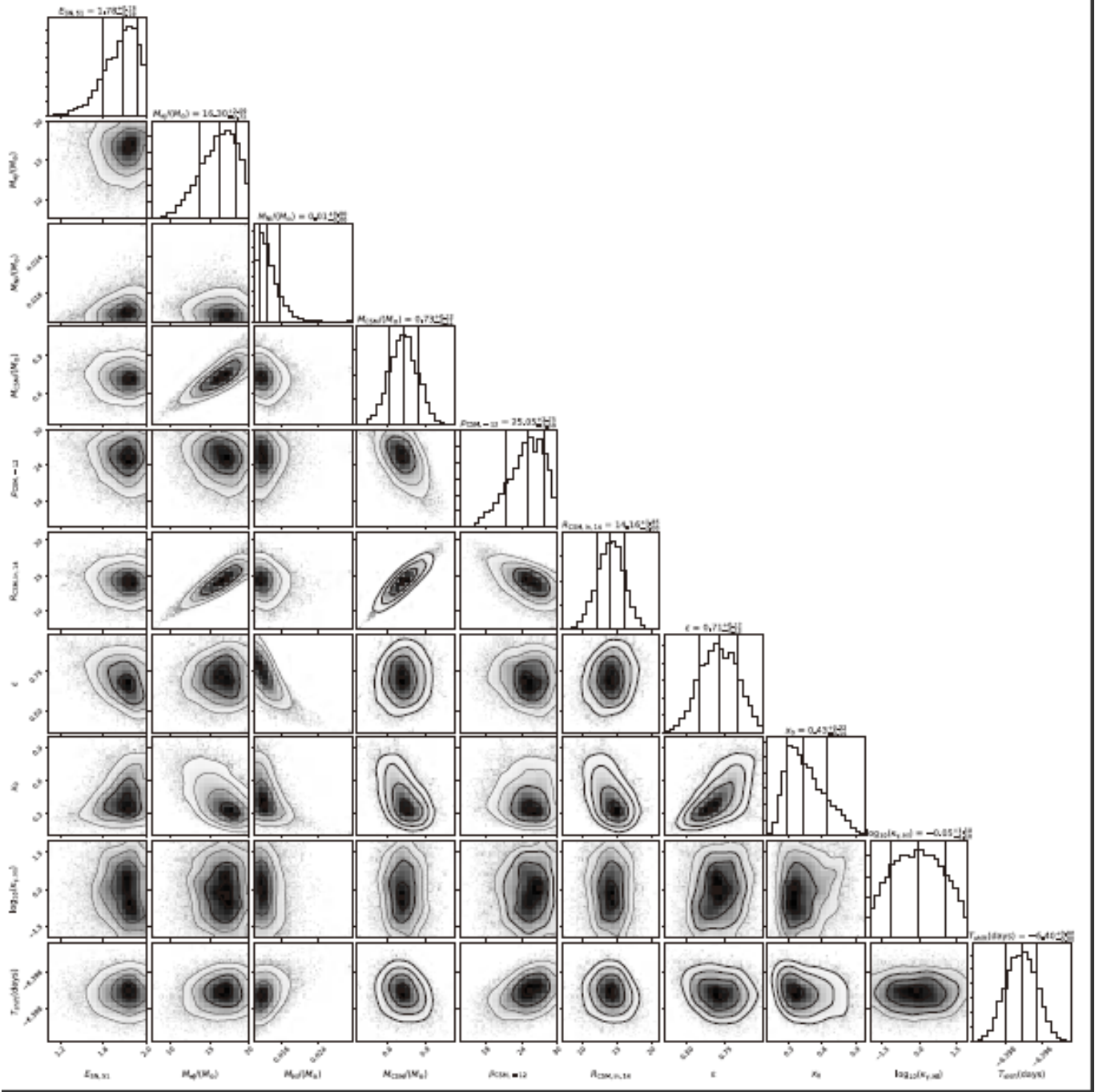


**Figure 14.** The corner plot of the  $^{56}\text{Ni}$  + CSI shell model displaying covariance of estimated parameters.

Chevalier, R. A., & Fransson, C. 1994, ApJ, 420, 268,  
doi: [10.1086/173557](https://doi.org/10.1086/173557)

Chugai, N. N., & Danziger, I. J. 1994, MNRAS, 268, 173,  
doi: [10.1093/mnras/268.1.173](https://doi.org/10.1093/mnras/268.1.173)

Cooke, J., Ellis, R. S., Nugent, P. E., et al. 2010, The  
Astronomer's Telegram, 2491, 1

Crowther, P., & Smartt, S. 2007, Astronomy and  
Geophysics, 48, 1.35,  
doi: [10.1111/j.1468-4004.2007.48135.x](https://doi.org/10.1111/j.1468-4004.2007.48135.x)

Fassia, A., Meikle, W. P. S., Chugai, N., et al. 2001,  
MNRAS, 325, 907, doi: [10.1046/j.1365-8711.2001.04282.x](https://doi.org/10.1046/j.1365-8711.2001.04282.x)

Foley, R. J., Smith, N., Ganeshalingam, M., et al. 2007,  
ApJL, 657, L105, doi: [10.1086/513145](https://doi.org/10.1086/513145)

- Fremling, C., Dugas, A., & Sharma, Y. 2019, Transient Name Server Classification Report, 2019-188, 1
- Gal-Yam, A. 2014, in American Astronomical Society Meeting Abstracts, Vol. 223, American Astronomical Society Meeting Abstracts #223, 235.02
- Gal-Yam, A., Arcavi, I., Ofek, E. O., et al. 2014, *Nature*, 509, 471, doi: [10.1038/nature13304](https://doi.org/10.1038/nature13304)
- Ginzburg, S., & Balberg, S. 2012, *ApJ*, 757, 178, doi: [10.1088/0004-637X/757/2/178](https://doi.org/10.1088/0004-637X/757/2/178)
- Gorbikov, E., Gal-Yam, A., Ofek, E. O., et al. 2014, *MNRAS*, 443, 671, doi: [10.1093/mnras/stu1184](https://doi.org/10.1093/mnras/stu1184)
- Hakobyan, A. A., Adibekyan, V. Z., Aramyan, L. S., et al. 2012, *A&A*, 544, A81, doi: [10.1051/0004-6361/201219541](https://doi.org/10.1051/0004-6361/201219541)
- Hosseinzadeh, G., McCully, C., Zabludoff, A. I., et al. 2019, *ApJL*, 871, L9, doi: [10.3847/2041-8213/aafc61](https://doi.org/10.3847/2041-8213/aafc61)
- Hosseinzadeh, G., Arcavi, I., Valenti, S., et al. 2017, *ApJ*, 836, 158, doi: [10.3847/1538-4357/836/2/158](https://doi.org/10.3847/1538-4357/836/2/158)
- Jordi, K., Grebel, E. K., & Ammon, K. 2006, *A&A*, 460, 339, doi: [10.1051/0004-6361:20066082](https://doi.org/10.1051/0004-6361:20066082)
- Karamahmetoglu, E., Fransson, C., Sollerman, J., et al. 2019, arXiv e-prints, arXiv:1910.06016, <https://arxiv.org/abs/1910.06016>
- Khazov, D., Yaron, O., Gal-Yam, A., et al. 2016, *ApJ*, 818, 3, doi: [10.3847/0004-637X/818/1/3](https://doi.org/10.3847/0004-637X/818/1/3)
- Liu, L.-D., Wang, L.-J., Wang, S.-Q., & Dai, Z.-G. 2018, *ApJ*, 856, 59, doi: [10.3847/1538-4357/aab157](https://doi.org/10.3847/1538-4357/aab157)
- Lusk, J. A., & Baron, E. 2017, *PASP*, 129, 044202, doi: [10.1088/1538-3873/aa5e49](https://doi.org/10.1088/1538-3873/aa5e49)
- Lyman, J. D., Bersier, D., James, P. A., et al. 2016, *MNRAS*, 457, 328, doi: [10.1093/mnras/stv2983](https://doi.org/10.1093/mnras/stv2983)
- Morozova, V., Piro, A. L., & Valenti, S. 2017, *ApJ*, 838, 28, doi: [10.3847/1538-4357/aa6251](https://doi.org/10.3847/1538-4357/aa6251)
- Munari, U., & Zwitter, T. 1997, *A&A*, 318, 269
- Nicholl, M. 2018, *Research Notes of the American Astronomical Society*, 2, 230, doi: [10.3847/2515-5172/aaf799](https://doi.org/10.3847/2515-5172/aaf799)
- Nyholm, A., Sollerman, J., Taddia, F., et al. 2017, *A&A*, 605, A6, doi: [10.1051/0004-6361/201629906](https://doi.org/10.1051/0004-6361/201629906)
- Pastorello, A., Smartt, S. J., Mattila, S., et al. 2007, *Nature*, 447, 829, doi: [10.1038/nature05825](https://doi.org/10.1038/nature05825)
- Pastorello, A., Mattila, S., Zampieri, L., et al. 2008, *MNRAS*, 389, 113, doi: [10.1111/j.1365-2966.2008.13602.x](https://doi.org/10.1111/j.1365-2966.2008.13602.x)
- Pastorello, A., Wyrzykowski, L., Valenti, S., et al. 2015a, *MNRAS*, 449, 1941, doi: [10.1093/mnras/stu2621](https://doi.org/10.1093/mnras/stu2621)
- Pastorello, A., Hadjiyska, E., Rabinowitz, D., et al. 2015b, *MNRAS*, 449, 1954, doi: [10.1093/mnras/stv335](https://doi.org/10.1093/mnras/stv335)
- Pastorello, A., Benetti, S., Brown, P. J., et al. 2015c, *MNRAS*, 449, 1921, doi: [10.1093/mnras/stu2745](https://doi.org/10.1093/mnras/stu2745)
- Pastorello, A., Prieto, J. L., Elias-Rosa, N., et al. 2015d, *MNRAS*, 453, 3649, doi: [10.1093/mnras/stv1812](https://doi.org/10.1093/mnras/stv1812)
- Pastorello, A., Wang, X. F., Ciabattari, F., et al. 2016, *MNRAS*, 456, 853, doi: [10.1093/mnras/stv2634](https://doi.org/10.1093/mnras/stv2634)
- Poznanski, D., Prochaska, J. X., & Bloom, J. S. 2012, *MNRAS*, 426, 1465, doi: [10.1111/j.1365-2966.2012.21796.x](https://doi.org/10.1111/j.1365-2966.2012.21796.x)
- Prentice, S. J., Mazzali, P. A., Pian, E., et al. 2016, *MNRAS*, 458, 2973, doi: [10.1093/mnras/stw299](https://doi.org/10.1093/mnras/stw299)
- Prentice, S. J., Ashall, C., James, P. A., et al. 2019, *MNRAS*, 485, 1559, doi: [10.1093/mnras/sty3399](https://doi.org/10.1093/mnras/sty3399)
- Sanders, N. E., Soderberg, A. M., Foley, R. J., et al. 2013, *ApJ*, 769, 39, doi: [10.1088/0004-637X/769/1/39](https://doi.org/10.1088/0004-637X/769/1/39)
- Schlaflly, E. F., & Finkbeiner, D. P. 2011, *ApJ*, 737, 103, doi: [10.1088/0004-637X/737/2/103](https://doi.org/10.1088/0004-637X/737/2/103)
- Schlegel, E. M. 1990, *MNRAS*, 244, 269
- Shivvers, I., Zheng, W. K., Mauerhan, J., et al. 2016, *MNRAS*, 461, 3057, doi: [10.1093/mnras/stw1528](https://doi.org/10.1093/mnras/stw1528)
- Silverman, J. M., Kleiser, I. K. W., Morton, A. J. L., & Filippenko, A. V. 2010, *Central Bureau Electronic Telegrams*, 2223, 1
- Smith, N., Foley, R. J., & Filippenko, A. V. 2008, *ApJ*, 680, 568, doi: [10.1086/587860](https://doi.org/10.1086/587860)
- Stetson, P. B. 1987, *PASP*, 99, 191, doi: [10.1086/131977](https://doi.org/10.1086/131977)
- Sun, N.-C., Maund, J. R., Hirai, R., Crowther, P. A., & Podsiadlowski, P. 2019, arXiv e-prints, arXiv:1909.07999, <https://arxiv.org/abs/1909.07999>
- Taddia, F., Stritzinger, M. D., Sollerman, J., et al. 2013, *A&A*, 555, A10, doi: [10.1051/0004-6361/201321180](https://doi.org/10.1051/0004-6361/201321180)
- Tody, D. 1986, *Society of Photo-Optical Instrumentation Engineers (SPIE) Conference Series*, Vol. 627, *The IRAF Data Reduction and Analysis System*, ed. D. L. Crawford, 733, doi: [10.1117/12.968154](https://doi.org/10.1117/12.968154)
- . 1993, *Astronomical Society of the Pacific Conference Series*, Vol. 52, *IRAF in the Nineties*, ed. R. J. Hanisch, R. J. V. Brissenden, & J. Barnes, 173
- Valenti, S., Fraser, M., Benetti, S., et al. 2011, *MNRAS*, 416, 3138, doi: [10.1111/j.1365-2966.2011.19262.x](https://doi.org/10.1111/j.1365-2966.2011.19262.x)
- Valenti, S., Sand, D., Pastorello, A., et al. 2014, *MNRAS*, 438, L101, doi: [10.1093/mnrasl/slt171](https://doi.org/10.1093/mnrasl/slt171)
- Valenti, S., Howell, D. A., Stritzinger, M. D., et al. 2016, *MNRAS*, 459, 3939, doi: [10.1093/mnras/stw870](https://doi.org/10.1093/mnras/stw870)
- Wang, S.-Q., & Li, L. 2019, arXiv e-prints, arXiv:1905.12623, <https://arxiv.org/abs/1905.12623>
- Zhang, J., Xing, L., & Wang, X. 2019, *The Astronomer's Telegram*, 12410